Solar Phys (2013) 285:391–410
DOI 10.1007/s11207-012-0103-9

Propagation of Fast Coronal Mass Ejections and Shock Waves Associated with Type II Radio-Burst Emission: An Analytic Study

P. Corona-Romero · J.A. Gonzalez-Esparza · E. Aguilar-Rodriguez

Received: 13 March 2012 / Accepted: 8 August 2012 / Published online: 27 September 2012

Abstract Coronal mass ejections (CMEs) are large-scale eruptive events in the solar corona. Once they are expelled into the interplanetary (IP) medium, they propagate outwards and "evolve" interacting with the solar wind. Fast CMEs associated with IP shocks are a critical subject for space weather investigations. We present an analytic model to study the heliocentric evolution of fast CME/shock events and their association with type II radio-burst emissions. The propagation model assumes an early stage where the CME acts as a piston driving a shock wave; beyond this point the CME decelerates, tending to match the ambient solar wind speed and its shock decays. We use the shock speed evolution to reproduce type II radio-burst emissions. We analyse four fast CME halo events that were associated with kilometric type II radio bursts, and *in-situ* measurements of IP shock and CME signatures. The results show good agreement with the dynamic spectra of the type II frequency drifts and the *in-situ* measurements. This suggests that, in general, IP shocks associated with fast CMEs evolve as blast waves approaching 1 AU, implying that the CMEs do not drive their shocks any further at this heliocentric range.

Keywords Coronal mass ejections, interplanetary · Coronal mass ejections, theory · Radio bursts, type II

Observations and Modelling of the Inner Heliosphere
Guest Editors: Mario M. Bisi, Richard A. Harrison and Noé Lugaz

P. Corona-Romero (✉) · J.A. Gonzalez-Esparza · E. Aguilar-Rodriguez
MEXART, Instituto de Geofisica, Unidad Michoacan, Universidad Nacional Autonoma de Mexico, antigua carretera a Patzcuaro # 8701 Ex-Hda. San Jose de la Huerta, Morelia, Michoacan 58089, Mexico
e-mail: piter.cr@gmail.com

J.A. Gonzalez-Esparza
e-mail: americo@geofisica.unam.mx

E. Aguilar-Rodriguez
e-mail: ernesto@geofisica.unam.mx

P. Corona-Romero
Posgrado en Ciencias de la Tierra, Universidad Nacional Autonoma de Mexico, Circuito de la investigacion Cientifica s/n, Ciudad Universitaria, Delegacion Coyoacan, 04510 Mexico City, Mexico

1. Introduction

Coronal mass ejections (CMEs) are complex events involving the release of large amounts of material, energy, and magnetic field from the Sun into the solar wind. They may also involve other solar phenomena, such as solar flares, solar energetic particles, solar radio bursts, and interplanetary (IP) shocks (Forsyth *et al.*, 2006; Webb and Gopalswamy, 2006). In general, CMEs propagate through the IP medium with initial velocities between 200 – 2000 km s^{-1} (Vourlidas *et al.*, 2000). Fast CMEs associated with IP shocks are the main cause of intense geomagnetic storms (*e.g.* Ontiveros and Gonzalez-Esparza, 2010, and references therein), making the propagation of fast CMEs and their shocks a crucial issue in space weather studies. As pointed out by Vršnak (2006, 2008), we need to grasp the physical mechanisms that govern the CME evolution to understand when, where, and how fast CMEs propagate and decelerate in the IP medium.

Recently white-light observations, combining data from LASCO, SMEI, and the *Heliospheric Imagers* (HIs), tracked a few CMEs from the Sun to 1 AU, helping us to increase our knowledge of the CME kinematics (*e.g.* Harrison *et al.*, 2008, Webb *et al.*, 2009a, 2009b, Liu *et al.*, 2010a, 2010b). However, in general, it is very difficult to fully track these events, so we need more observations and developments to address this problem. There are several theoretical, numerical, and empirical studies to describe the CME dynamics (Forbes *et al.*, 2006). CMEs interact with the ambient solar wind, and this interaction decelerates (accelerates) the fast (slow) CMEs (Gopalswamy *et al.*, 2000). In general, analytical models focus on the dynamics in the CME–solar wind interaction; such as linear and quadratic drag forces (Cargill, 2004; Vršnak and Gopalswamy, 2002), mass accretion (Tappin, 2006), and viscous and turbulent forces (Borgazzi *et al.*, 2009). All these models assume a direct interaction between the CME and the ambient solar wind without taking into account the role of the driven IP shock and its plasma sheath (shocked solar wind).

It is possible to track fast CME/shock events using electromagnetic wave observations by spacecraft. Solar radio bursts of type II are characterised by a narrow band of intense radiation of which frequency drifts downwards with time and distance from the Sun over time scales from a few hours to one or two days. Type II bursts are produced by the excitation of plasma waves by a shock propagating through the solar wind (Cane and Stone, 1984; Cane, Sheeley, and Howard, 1987). These emissions occur at the fundamental and/or harmonic of the plasma frequency (f_{p}) which is related to the square root of the electron plasma density (n) at the source region (see Equation (16)). The type II radio bursts are typically observed in the metre-wave regime at frequencies less than 150 MHz. However, type II radio bursts have been observed to start at frequencies as high as 500 MHz (Nakajima *et al.*, 1990; Vršnak *et al.*, 1995). It is well established that decametric/hectometric (DH) to kilometric (km) type II radio emissions are caused by the propagation of fast CME/shocks through the interplanetary medium (Cane, Sheeley, and Howard, 1987). However, not necessarily all the CME/shock events generate type II emissions (Gopalswamy *et al.*, 1998, 2008). The type II frequency-drifting can, in principle, provide continuous tracking of some CME/shock events from the solar corona through the heliosphere. Therefore, these radio observations can be used to approximate the speed profile of a CME/shock (Reiner, Kaiser, and Bougeret, 2007). Furthermore, Gonzalez-Esparza and Aguilar-Rodriguez (2009) used the type II frequency drifts to calculate shock speeds, at some convenient intervals, tracking the shock deceleration in the IP medium; Lara and Borgazzi (2009) calculated the synthetic type II radio burst associated with the analytic trajectory of a CME using an analytic model.

Empirical studies on the propagation of IP shocks and fast CMEs point out relationships between shock arrival speeds, shock transit times, CME properties, and solar wind characteristics (*e.g.* Gopalswamy *et al.*, 2005; Kim, Moon, and Cho, 2007). However, when they are tested against several case events, the empirical models obtain large uncertainties, suggesting that we require a different perspective to address this problem (Cho *et al.*, 2003; Kim, Moon, and Cho, 2007).

Dryer (1974) studied blast shocks associated with solar flares from analytical and numeric perspectives. Smart and Shea (1985) also investigated IP shocks related to solar flares, they found that IP shocks propagation presents two stages:

i) a short period of constant speed where the shock is driven by a piston for which speed and duration were derived from metric type II bursts and solar flare intensity, and
ii) a blast wave decaying evolution.

Pinter and Dryer (1990) applied these results to calculate transit times (TT) to 1 AU of some shocks associated with solar flares, obtaining good agreement with observations. They also found that the characteristics of the driving stage affect the shock TT and arrival speed. On the other hand, there are reports of a similar heliocentric evolution in shocks associated with fast CMEs. Combining coronagraph, interplanetary scintillation and *in-situ* measurements, Manoharan *et al.* (2001), Manoharan (2006, 2010) and Pohjolainen *et al.* (2007) tracked the propagation of some fast CME/shock events, suggesting that they also present two propagation stages within 1 AU: an initial one, near the Sun, with a small deceleration up to a certain heliocentric distance, beyond which there is a large deceleration where the CME/shock tends to equal the ambient wind speed.

These two propagation stages in the heliocentric evolution of fast CME/shock events are also found in numerical and analytical models. González-Esparza *et al.* (2003a, 2003b, 2007) developed 1D hydrodynamic (HD) numerical simulations of fast CMEs in the IP medium. They found that a fast CME front and its shock present an initial quasi-constant speed propagation followed by a decaying speed at farther heliocentric distances. On the other hand, Cantó *et al.* (2005) presented a full analytic HD model to calculate CME trajectories and TTs. This model also finds the two propagation stages. Corona-Romero and Gonzalez-Esparza (2011) investigated the similarities between the numerical and analytical models commented on before. They concluded that the evolution of a fast CME/shock is described by three dynamic phases: *driving*, *decoupling*, and *decaying*. In the driving phase, the fast CME propagates with a quasi-constant speed, a condition which allows it to transfer momentum forward, driving the shock. On the other hand, in the final decaying stage, the fast CME decelerates, tending to equal the ambient wind speed and its shock evolves as a blast wave slowing to become a magnetosonic perturbation. The intermediate decoupling phase bonds these two opposite dynamic states, implying a ceasing transfer of momentum through the plasma sheath, from the CME front to the shock.

We study the propagation of fast CME/shock events, to compare the evolution of the shock speed with type II radio burst drifts and *in-situ* measurements. In order to do so, we start from a piston-shock analytical model to describe the CME and shock evolutions. We modify this model to adapt it to more realistic scenarios (Section 2). In Section 3 we apply the model to analyse four study cases, calculating the trajectories of CMEs, IP shocks, and simulating the type II radio-burst emission associated with the shock propagation. Finally, we present our summary and conclusions in Section 4.

2. Analytical Model of Fast CME/Shock Propagation

Cantó, Raga, and D'Alessio (2000) developed an analytical formalism to describe the dynamics of two interacting hypersonic fluids; such a formalism was based on the conservation

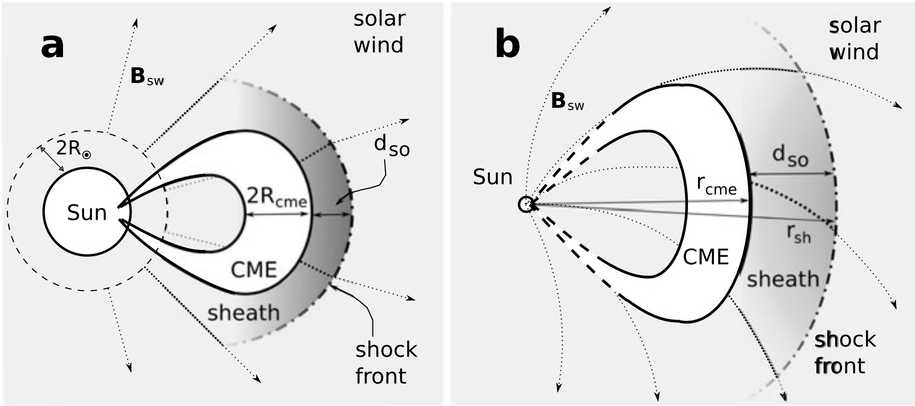

Figure 1 CME/shock model for times (a) $t < \tau_{c1}$ and (b) $t > \tau_{c2}$. The croissant-like shape represents the fast CME with radius R_{cme} and the shock is propagating ahead. The dotted thin lines represent the magnetic field lines. r_{cme} and r_{sh} are the heliocentric positions of the CME leading edge and the shock, respectively. The separation between the CME front and the shock is the standoff distance (d_{so}). (a) During the driving stage ($t < \tau_{c1}$) the CME and shock wave have the same speed and d_{so} is almost constant. (b) In the decaying stage ($t > \tau_{c2}$) the CME decelerates, tending to equal the solar wind speed, and the shock wave decays to become a magnetosonic perturbation, d_{so} increases and the plasma sheath expands and relaxes into normal solar wind.

of linear momentum. Subsequently, Cantó *et al.* (2005) adapted this formalism to describe the propagation of supersonic CMEs through the solar wind (SW). They considered the CME as a dense and fast fluid injected into the ambient wind. The SW opposition to the CME propagation derives into the CME deceleration by the equilibrium of linear momentum between the CME and ambient wind. The CME is injected at an initial position (beyond the critical point) during the injection time. In the present work we use the notation Δt_f and r_0 for the injection time and the initial position, respectively.

Based on the previously discussed work, Corona-Romero and Gonzalez-Esparza (2011) developed a piston-shock analytical HD model to describe the evolution of the CME driver and its shock in the inner heliosphere. They compared their model with 1D HD numerical simulations of CME/shock events. In the analytical model they assumed the pristine fast CME as a piston driving a shock wave, and they obtained analytical expressions for the shock propagation. They found good agreement between the model and simulations. The two models show that initially the fast CME propagates at about a constant speed and drives the shock (driving stage) until it reaches a certain distance after which it decelerates and decouples from the shock (decoupling process). Then the CME and its shock decelerate (decaying stage). They also applied the piston shock model to analyse a few fast CME/shock events finding quantitative agreement with CME *in-situ* data at 1 AU; however, the shock arrival speeds and their TTs presented some discrepancies with the *in-situ* observations. They concluded that these inconsistencies could be explained by neglecting the tangential flows inside the plasma sheath. This 1D condition overestimates the plasma-sheath width and the shock speed, thereby causing shorter shock TTs.

Now we extend the model starting from a driver bow shock initial configuration for the fast CME/shock (Ontiveros and Vourlidas, 2009; Vourlidas and Ontiveros, 2009; Maloney and Gallagher, 2011). Figure 1a shows a sketch of the model, the croissant-like CME and the shock wave. The shadow region between the CME leading edge (r_{cme}) and the shock (r_{sh}) is the plasma sheath, formed by compressed solar wind. Such geometry considers the tangential mass fluxes inside the plasma sheath, since the sheath material flows around the CME, solving the problems commented on in the previous paragraph.

We consider the solar wind as a spherically homogeneous polytropic plasma (with polytropic index γ) expanding at a constant rate. Frozen in the solar wind there is a magnetic field initially radial at two solar radii ($R_\odot$), and the field source rotates with a frequency $\omega_\odot = 2.7 \times 10^{-6}$ Hz (solar sidereal period at the equator). Figure 1 shows the magnetic field configuration (dotted thin lines); in panel (a) the magnetic field is radial near the Sun, while the field lines are curved at larger heliocentric distances (panel (b)).

2.1. CME Propagation

Following Corona-Romero and Gonzalez-Esparza (2011), at the beginning, during the driving stage, the CME leading edge maintains a constant speed. The first critical time (τ_{c1}) indicates the time when the interaction with the plasma sheath becomes dominant, causing the deceleration of the CME. Thus τ_{c1} splits the evolution of the CME speed (v_{cme}):

$$v_{\mathrm{cme}}(t) = \begin{cases} v_{0\mathrm{cme}}, & t < \tau_{c1}, \\ v_{1\mathrm{AU}}\left(1 + \frac{(a-1)\sqrt{ac}\Delta t_f}{\sqrt{2(a-1)\Delta t_f t - a(1-c)(\Delta t_f)^2}}\right), & t \geq \tau_{c1}, \end{cases} \tag{1}$$

where $v_{0\mathrm{cme}}$ is the speed near the Sun (linear fit of plane-of-sky speed measured by coronagraph images), $v_{1\mathrm{AU}}$ is the solar wind speed at 1 AU, and Δt_f the duration of the rise phase associated with the flare. In addition, τ_{c1} is defined by

$$\tau_{c1} = \frac{a(1+\sqrt{c})}{a-1}\Delta t_f, \tag{2}$$

where a and c are related with the CME kinetic properties. a can be expressed by

$$a = \frac{v_{0\mathrm{cme}}}{v_{1\mathrm{AU}}}\left(\frac{1+\sqrt{c}}{\sqrt{c}}\right) - \frac{1}{\sqrt{c}}, \tag{3}$$

and

$$c = \frac{n_{0\mathrm{cme}}}{n_{1\mathrm{AU}}}\left(\frac{r_{0\mathrm{cme}}}{1\ \mathrm{AU}}\right)^2. \tag{4}$$

c is the ratio between the CME ($n_{0\mathrm{cme}}$) and the local solar wind ($n_{1\mathrm{AU}}[1\ \mathrm{AU}/r_{0\mathrm{cme}}]^2$) densities at $t = 0$; here $r_{0\mathrm{cme}}$ and $n_{1\mathrm{AU}}$ are the initial position of the CME leading edge and the solar wind density at 1 AU, respectively.

The product $acn_{1\mathrm{AU}}v_{1\mathrm{AU}}$ represents the flux of injected CME material during the interval Δt_f. The constants a and c are related with the CME initial inertia and kinetic energy, and they are also related with the ambient SW characteristics at the inner boundary (Equations (3) and (4)). For these reasons, the CME dynamics depends on the values of a, c and Δt_f, which define the duration of driving and decaying phases (Equation (2)) as well the CME deceleration (see Equation (1)).

Finally, the CME leading edge position (r_{cme}) is obtained by integrating Equation (1):

$$r_{\mathrm{cme}}(t) = \begin{cases} r_{0\mathrm{cme}} + v_{0\mathrm{cme}}t, & t < \tau_{c1}, \\ r_{0\mathrm{cme}} + v_{1\mathrm{AU}}(t - ac\Delta t_f) & \\ \quad + v_{1\mathrm{AU}}\sqrt{2(a-1)ac\Delta t_f t - a^2c(1-c)(\Delta t_f)^2}, & t \geq \tau_{c1}. \end{cases} \tag{5}$$

Further details of this model and its applications can be found in González and Cantó (2002) and González *et al.* (2006).

2.2. Shock Propagation

The shock begins its propagation as a bow shock *driven* by the CME (see Figure 1a). During the driving stage ($t < \tau_{c1}$) the CME speed (v_{cme}) is constant and the ratio between the standoff distance (d_{so}) and the CME radius (R_{cme}) depends on the magnetosonic Mach number (M_1) and γ (Maloney and Gallagher, 2011 and references therein). The shorter M_1 the larger $d_{\mathrm{so}}/R_{\mathrm{cme}}$. For large values of M_1, $d_{\mathrm{so}}/R_{\mathrm{cme}}$ tends to an asymptotic value (~ 0.23) determined by γ (Petrinec, 2002). During the driving stage M_1 increases due to the solar wind expansion and the constant value of v_{cme}; this decreases the value of $d_{\mathrm{so}}/R_{\mathrm{cme}}$. However, the CME expansion may reduce this effect making the value of d_{so} relatively constant. For simplicity, we assume that d_{so} is constant during the driving; implying that, for $t < \tau_{c1}$, the CME leading edge and shock speeds are equal ($v_{\mathrm{cme}} = v_{\mathrm{sh}}$).

For times $t > \tau_{c1}$ the CME and shock speeds begin to differ due to the CME deceleration, which increases the distance between the CME front and the shock. As this distance grows, the driving from the CME gradually ceases. Then, a time comes when the plasma-sheath relaxation leads to the end of the driving stage. The second critical time (τ_{c2}) marks the moment when the CME is no longer capable to drive the bow shock, and consequently the shock begins to decouple and evolve into a blast wave. Figure 1b shows the decaying phase ($t > \tau_{c2}$), where the CME/shock standoff distance is growing. During this phase the shock fades out and the compression of the plasma sheath decreases.

The evolution of the shock speed (v_{sh}) is given by

$$v_{\mathrm{sh}}(t) = \begin{cases} v_{0\mathrm{cme}}, & t < \tau_{c2}, \\ (v_{0\mathrm{cme}} - v_{1\mathrm{AU}})(\frac{t}{\tau_{c2}})^{-1/3} + v_{1\mathrm{AU}}, & t \geq \tau_{c2}. \end{cases} \tag{6}$$

During the first stage of Equation (6), the shock is driven by the CME; the second stage ($t \geq \tau_{c2}$) is the blast wave solution for a r^{-2} density profile (Cavaliere and Messina, 1976). Moreover, τ_{c2} is defined as

$$\tau_{c2} = \frac{d_{\mathrm{so}}}{\sqrt{c_{A2}^2 + c_{S2}^2}} + \tau_{c1}, \tag{7}$$

where c_{A2} and c_{S2} are the Alfvénic and sonic speeds in the plasma sheath at $t = \tau_{c1}$. The values for c_{A2} and c_{S2} are calculated as

$$c_{A2}^2 = c_{A1}^2 \left[\frac{B_*^2}{n_*} \right], \tag{8}$$

$$c_{S2}^2 = c_{S1}^2 \left[\frac{p_*}{n_*} \right], \tag{9}$$

where c_{A1} and c_{S1} are the Alfvénic and sonic speeds, respectively. The magnetic field (B_*), number density (n_*) and thermal pressure (p_*) jumps across the shock are calculated by the Petrinec and Russell (1997) polytropic jump relations (see the Appendix, Equations (20), (19), and (21)).

To calculate d_{so} in Equation (7), we combine the Bothmer and Schwenn (1998) empirical relation to estimate the CME radius (R_{cme}) and the Farris and Russell (1994) model to approach the standoff distance. After some manipulation, we obtain a relation between r_{cme} and d_{so}:

$$\frac{d_{\mathrm{so}}}{1\ \mathrm{AU}} = 0.264 \left[\frac{(\gamma - 1)M_1^2 + 2}{(\gamma + 1)(M_1^2 - 1)} \right] \left(\frac{r_{1\mathrm{cme}}}{1\ \mathrm{AU}} \right)^{0.78}, \tag{10}$$

where $r_{1\mathrm{cme}} = r_{0\mathrm{cme}} + v_{0\mathrm{cme}}\tau_{c1}$ is the CME leading edge position at $t = \tau_{c1}$. M_1 is defined by

$$M_1^2 = \frac{2(v_{0\mathrm{cme}} - v_{1\mathrm{AU}})^2}{c_{A1}^2 + c_{S1}^2 + \sqrt{(c_{A1}^2 + c_{S1}^2)^2 - 4\cos^2(\theta_{Bv}) c_{A1}^2 c_{S1}^2}}, \tag{11}$$

with θ_{Bv} the angle between the IP magnetic field ($\mathbf{B}_{\mathrm{sw}}$) and the shock normal.

The values of c_{A1}, c_{S1}, and θ_{Bv} are calculated by

$$c_{A1}^2 = \frac{B_{1\mathrm{AU}}^2}{\mu_0 n_{1\mathrm{AU}}} \left[\frac{1\ \mathrm{AU}}{r_{1\mathrm{cme}}}\right]^2 \left[\frac{v_{1\mathrm{AU}} + (r_{1\mathrm{cme}} - 2R_\odot)\omega_\odot}{v_{1\mathrm{AU}} + (1\ \mathrm{AU} - 2R_\odot)\omega_\odot}\right], \tag{12}$$

$$c_{S1}^2 = \gamma \frac{2k_B T_{1\mathrm{AU}}}{m_p} \left[\frac{1\ \mathrm{AU}}{r_{1\mathrm{cme}}}\right]^{2(\gamma-1)}, \tag{13}$$

$$\cos^2(\theta_{Bv}) = \frac{v_{1\mathrm{AU}}^2}{v_{1\mathrm{AU}}^2 + (r_{1\mathrm{cme}} - 2R_\odot)^2 \omega_\odot^2}, \tag{14}$$

where $n_{1\mathrm{AU}}$, $B_{1\mathrm{AU}}$, and $T_{1\mathrm{AU}}$ are the values of proton density, magnetic field intensity, and proton temperature at 1 AU, respectively. In Equation (13) we consider an equal number of protons and electrons, and in Equations (12), (13) and (14) we apply the frozen-in Parker-like magnetic field assumption.

Finally, the shock position (r_{sh}) is obtained by integrating Equation (6):

$$r_{\mathrm{sh}}(t) = \begin{cases} v_{0\mathrm{cme}} t + r_{0\mathrm{cme}} + d_{\mathrm{so}}, & t < \tau_{c2}, \\ \frac{3}{2}(v_{0\mathrm{cme}} - v_{1\mathrm{AU}})\tau_{c2}[(\frac{t}{\tau_{c2}})^{2/3} - 1] & \\ \quad + v_{1\mathrm{AU}}\tau_{c2}(\frac{t}{\tau_{c2}} - 1) + v_{0\mathrm{cme}}\tau_{c2} + r_{0\mathrm{cme}} + d_{\mathrm{so}}, & t \geq \tau_{c2}. \end{cases} \tag{15}$$

Equations (1), (5), (6) and (15) calculate speed and position of the CME and its shock.

3. Study Cases

We analysed seven fast ($v_{0\mathrm{cme}} > 1000\ \mathrm{km\,s^{-1}}$) halo CME events during 1996–2009. The CMEs were associated with solar flares, and their IP shocks were related to type II kilometric radio bursts emissions. The events were reported in both LASCO (Gopalswamy *et al.*, 2009) and Richardson and Cane (2010) lists. Table 1 shows the events and the initial conditions (and the solar wind at 1 AU) that we used in our calculations.

We applied the model described in the previous section to calculate the CME leading edge and shock trajectories. We require as initial conditions: the CME position (r_0) and speed ($v_{0\mathrm{cme}}$), and the flare rise time (Δt_f). The solar wind conditions at 1 AU were defined by using average values of *in-situ* measurements by the *Wind* spacecraft around six hours upstream of the shock signatures. The polytropic index was $\gamma = 1.5$. On the other hand, the initial density ratio (c) of the CME/solar wind at the inner boundary was a free parameter, the value of which was selected to equal the CME arrival time (Corona-Romero and Gonzalez-Esparza, 2011).

We simulated the type II frequency drifts associated with the propagation of the IP shocks using the CME/shock trajectory for our four best events (see Table 1). These radio emissions are electromagnetic waves emitted by the solar wind electrons perturbed by an external agent. The radiation frequency or plasma frequency (f_{p}) is given by

$$f_{\mathrm{p}}(t) = \sqrt{\frac{e^2 n_{1\mathrm{AU}}}{4\pi^2 \epsilon_0 m_{\mathrm{e}}} \left[\frac{1\ \mathrm{AU}}{r_{\mathrm{sh}}(t)}\right]}, \tag{16}$$

Table 1 List of events and initial conditions. From left to right: number; date; CME time; CME–solar wind initial density ratio (Equation (4)); CME position; CME plane of the sky speed; solar flare rise time (CME injection time); *in-situ* solar wind values for bulk speed, density, temperature of protons, and magnetic field magnitude, respectively.

Event			Initial conditions				‡Solar wind (at ∼ 1 AU)			
#	⋆Date	⋆Hour [UT]	c	⋆r_0 [$R_\odot$]	⋆$v_{0\mathrm{cme}}$ [km s^{-1}]	†Δt_f [h]	$v_{1\mathrm{AU}}$ [km s^{-1}]	$n_{1\mathrm{AU}}$ [cm^{-3}]	$T_{1\mathrm{AU}}$ [kK]	$B_{1\mathrm{AU}}$ [nT]
1	2000-06-06	15:54	23.0	3.98	1119.3	0.40	510.0	4.3	180	5.9
2	2000-07-14	10:54	11.0	5.21	1674.0	0.45	600.0	2.5	120	4.5
3	2001-04-26	12:30	4.0	4.83	1006.0	1.50	440.0	2.1	60	6.0
4	2001-11-04	16:35	10.0	4.41	1810.0	0.23	330.0	3.3	15	7.0
5	2001-11-22	23:30	2.9	4.77	1437.0	1.40	430.0	5.5	160	7.0
6	2003-10-29	20:54	8.3	2.92	2029.1	0.54	450.0	2.0	150	9.0
7	2005-05-13	17:12	11.0	4.57	1689.0	0.40	410.0	3.5	110	5.5

⋆ LASCO CME catalog (http://cdaw.gsfc.nasa.gov/CME_list/).

† GOES registers (http://www.swpc.noaa.gov/Data/goes.html).

‡ Detected *in-situ* by *Wind* (http://omniweb.gsfc.nasa.gov/).

where e is the fundamental charge, and m_e the electron mass. Given a value for $n_{1\mathrm{AU}}$, Equation (16) relates a simulated radio emission (f_p) to the shock propagation (r_sh). We used this equation and its first harmonic ($2f_\mathrm{p}$) to compare it with the type II radio spectra detected by the WAVES experiment (Bougeret *et al.*, 1995) on-board the *Wind* spacecraft.

Table 2 shows the comparison, for the seven CMEs, between the model results and the *in-situ* data at 1 AU. Columns 2 and 3 show the arrival speed of CMEs and shocks, and columns 4 and 5 show their TTs. Columns 6 and 7 show the critical times and distances (τ_{c1}, τ_{c2}, d_{c1}, d_{c2}) indicating the driving and decaying phases in the heliocentric evolution of the CMEs and their shocks (Equations (2) and (7)).

3.1. Case Study 1: Event on 6 June 2000

This event was detected by LASCO/C2 on 6 June 2000 at 15:54 UT; it was associated with an X2.3 solar flare. The CME reached 1 AU on 8 June at 12.00 UT. Figure 2a shows the CME and shock speed evolution as obtained from the model. At the beginning (driving phase), the CME (thin curve) and its shock (thick curve) propagate with a constant speed equal to the LASCO linear fit (open diamond). This constant speed lasts until τ_{c1} (vertical dashed line), after which the CME decelerates. The shock speed is constant until τ_{c2} (vertical dotted line); for longer times, the shock decelerates (decaying phase). Note that the calculated CME and shock arrival speeds (solid circumferences) are very close to the *in-situ* measurements. Figure 2b shows the CME and shock trajectories as given by the model. At the beginning, the CME matches the LASCO data (diamonds). As commented on before, due to the arbitrary selection of c, the calculated CME transit time (open circle) matches the *in-situ* measurement (cross); the calculated shock arrival (open circle) occurs two hours earlier than the *in-situ* register (plus sign). Figure 2c shows the *Wind*/WAVES (Bougeret *et al.*, 1995) dynamic spectrum during the period of time where the event is propagating. We notice a type II radio burst, drifting from about 14 MHz down to 40 kHz. At the beginning of the emission, a fundamental–harmonic (FH) pair is observed; then a single tone, sometimes very intense, is drifting to lower frequencies. Overplotted on the dynamic spectrum

Table 2 Comparison of *in-situ* measurements and model results. (1) CME front and shock speeds at 1 AU; (2) CME front and shock transit times; (3) CME/shock critical times (τ) and critical distances (d).

Event	(1) Arrival speeds		(2) Transit times (TT)		(3) Driving and decaying	
	v_{cme} [km s^{-1}]	v_{sh} [km s^{-1}]	CME [h]	shock [h]	τ_{c1}-d_{c1} [h]-[R$_\odot$]	τ_{c2}-d_{c2} [h]-[R$_\odot$]
1	770⋆/795	871†/865	44.1⋆/44.3	41.3⋆/39.4	3.9-26.7	7.9-49.8
2	1000⋆/1035	1120†/1153	32.1⋆/32.1	27.7⋆/29.1	2.7-28.8	4.1-40.6
3	700⋆/688	812†/832	49.5⋆/49.7	40.5⋆/39.6	6.8-40.4	13.6-75.8
4	730⋆‡/660	‡/881	43.6⋆/45.5	33.4⋆/35.6	1.1-15.3	1.9-22.7
5	700⋆/823	1008†/994	37.5⋆/38.54	30.4⋆/33.3	4.7-39.6	6.2-50.1
6	1040⋆‡/1074	‡/1264	28.9⋆/29.1	21.22⋆/25.4	2.54-29.6	3.69-41.7
7	900⋆/848	942†‡/982	36.8⋆/37.0	33.4⋆/33.0	2.2-23.4	3.2-32.6

⋆ *Wind* measurements and Richardson and Cane (2010) catalogue.

† Calculated using the velocity coplanarity (see the Appendix, Equation (22)) and *Wind in-situ* data.

‡ Data gap.

Analytical results: $d_{c1} = v_{0\mathrm{cme}}\tau_{c1} + r_0$, and $d_{c2} = v_{0\mathrm{cme}}\tau_{c2} + r_0$.

are the calculated fundamental plasma frequency (solid line) and its first harmonic (dashed line). We see then that the first harmonic is qualitatively consistent with the lower part of the emission band.

3.2. Case Study 2: Event on 14 July 2000

The Bastille day event appeared in LASCO/C2 on 14 July 2000 at 10:54 UT, and it was associated with a X5.7 flare. The CME arrived at 1 AU on 15 July at 19:00 UT. This event is particularly difficult to study due to the multiple CME arrivals from 10 July to 15 July; in fact, another CME passed by the Earth neighbourhood (15:32 UT) just a few hours before the event arrival (Richardson and Cane, 2010). These circumstances complicated the acquisition of solar wind data and affected the CME/shock evolution by generating interactions between the CME and the previous disturbances. Nevertheless, the general results are similar to those obtained in the previous case showing quantitative and qualitative agreement with data. Figure 3a shows the evolution of CME and shock speeds as inferred from the model. We can appreciate the two phases (driving–decaying) in both speed profiles. The critical times (t_{c1} and t_{c2}) are shorter than in the previous case (see Table 2). The calculated CME arrival speed matches with the *in-situ* data; whereas the analytical shock arrival speed is faster than its *in-situ* counterpart. Figure 3b presents the CME leading edge and shock positions. Close to the Sun, the CME leading edge matches the LASCO data (diamonds). The estimated CME transit time (open circle) matches the *in-situ* measurement (cross); the calculated shock arrival (open circle) occurs about one hour earlier than the *in-situ* measurement (plus sign). Figure 3c shows the dynamic spectrum associated with the event. We notice that the type II radio burst is contaminated with a type III storm as a result of the solar activity, before and after the event. Similar to the previous case study, the calculated first harmonic (dashed line) is qualitatively consistent with the lower part of the emission band.

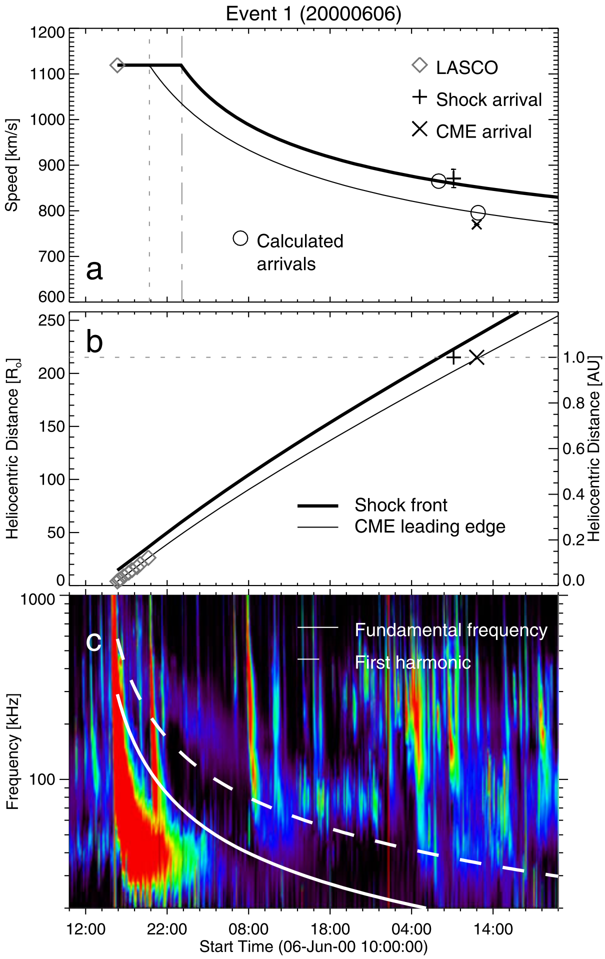

Figure 2 Case study 1: comparison of model results and observations. (a) Evolution of CME (thin line) and shock speeds (thick line) as deduced from the analytical model. Vertical dashed and dash-dotted gray lines indicate τ_{c1} and τ_{c2}, respectively (see Table 2). (b) CME (thin line) and shock (thick line) trajectories as deduced from the model. The symbols indicate the *in-situ* measurements from the *Wind* spacecraft, and the horizontal dotted line indicates 1 AU. (c) Type II dynamic radio spectra detected by *Wind*/WAVES, and computed fundamental plasma frequency (solid line) and first harmonic (dashed line) as deduced from the model (see text).

3.3. Case Study 3: Event on 26 April 2001

This event was detected by LASCO/C2 on 26 April 2001 at 12:30 UT, and it was associated with an M7.8 X-ray solar flare. The CME arrived at 1 AU on 28 April at 14:00 UT. Figure 4a shows the two propagation stages, we also appreciate coincidences between the radio data and the calculated shock propagation. The calculated arrival speeds for the CME leading edge and its shock are very close to their *in-situ* counterparts. Figure 4b shows that the CME leading edge position matches with most of the LASCO data, and the calculated shock TT is quite similar to the *in-situ* measurements (less than one hour of difference). Figure 4c shows the dynamic spectrum during the period of time when the event is taking place. We notice that the type II radio burst is extremely chaotic, drifting from about $\sim$5 MHz down to $\sim$20 kHz. Moreover, there is a $\sim$nine hour gap in the dynamic spectrum on 26 April. Overplotted on the dynamic spectrum are the calculated fundamental plasma frequency (solid line) and its first harmonic (dashed line). We see that the first harmonic is qualitatively consistent with the lower part of the type II emission band.

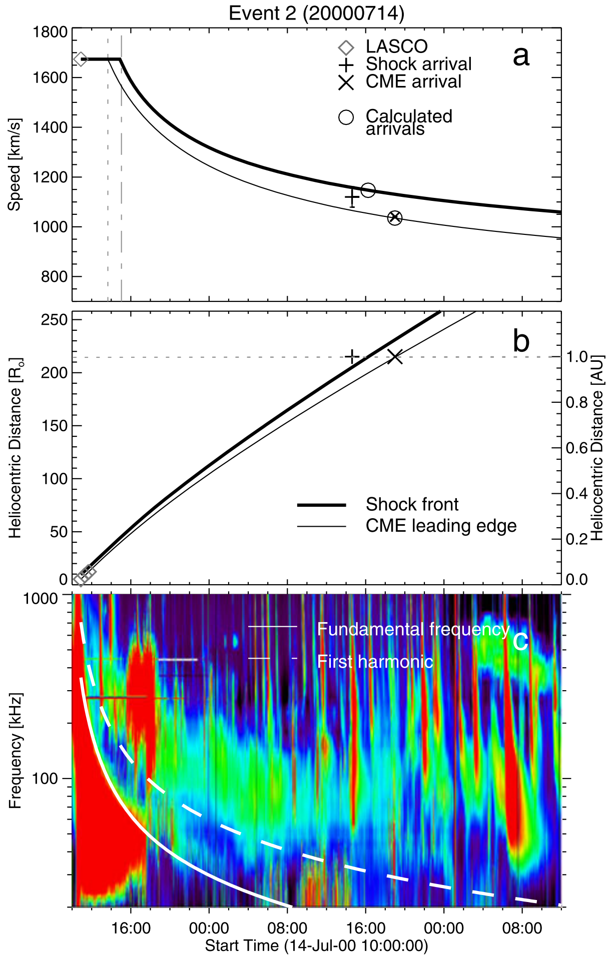

Figure 3 Case study 2: Bastille day event 2000, comparison of model results and observations. Same format as in Figure 2.

3.4. Case Study 4: Event on 13 May 2005

This event was detected in LASCO/C3 on 13 May 2005 at 17:12 UT and was associated with a M8.0 flare; the CME arrived at 1 AU in 15 May at 06:00 UT. Figure 5 shows the two phases in the CME and shock speeds. We also observe that the CME and shock evolutions are consistent with coronagraph and *in-situ* data. The arrival speeds and TTs of the CME and its shock are quantitative similar to the *in-situ* values. Figure 5c shows that the calculated first harmonic closely follows the lower part of the type II emission associated with the shock, from the beginning of the event up to 02:00 UT on 15 May.

This event was analysed in detail by Bisi *et al.* (2010), who report a CME/shock deceleration as the event evolved from near the Sun to 1 AU. Figure 5 shows qualitative agreement with this interpretation. However, a direct comparison between our analytic results and the speed data points (Figure 35 in Bisi *et al.*, 2010) is difficult. The speed analysis by Bisi *et al.* presents a significant dispersion, which, as the authors point out, might be due to the fact that the speed data points were associated with different regions at different times of the CME/shock event.

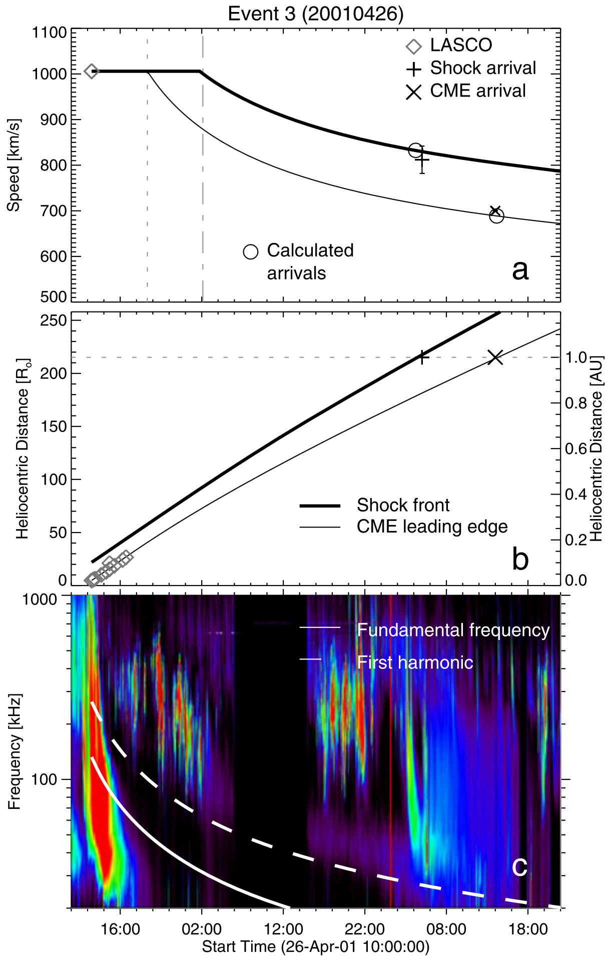

Figure 4 Case study 3: comparison of model results and observations. Same format as in Figure 2.

4. Discussion

We present an analytical model for approximate fast CME/shock propagation based on the dynamics of an ejecta driver and a driven shock wave. According to our model there are two main stages:

i) The driving phase ($0 < t < \tau_{c1}$), when the CME drives the shock wave and the separation between the CME leading edge and its shock is about constant.
ii) The decaying phase ($t > \tau_{c2}$), when the CME tends to equal the solar wind speed, the shock wave evolves into a blast wave, and the separation between the CME leading edge and the shock front increases.

As initial conditions, our model requires: CME initial speed ($v_{0\mathrm{cme}}$), position ($r_{0\mathrm{cme}}$), density ($n_{0\mathrm{cme}}$), injection time (Δt_f) and the ambient solar wind conditions. In order to apply our model to study fast CMEs propagating to the Earth, we used $v_{0\mathrm{cme}}$ and $r_{0\mathrm{cme}}$ from coronagraph images (LASCO observations), Δt_f from the flare rise phase (soft X-ray fluxes), and the solar wind conditions from *in-situ* measurements at 1 AU assuming a radial

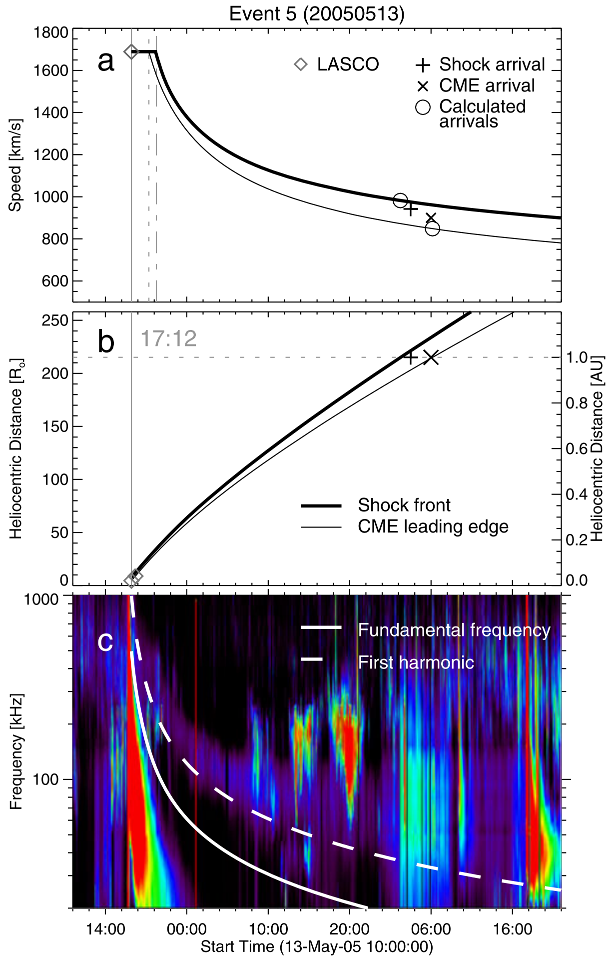

Figure 5 Case study 4: comparison of model results and observations. Same format as in Figure 2.

expansion. The initial CME density (Equation (4)) is our only free parameter, which was chosen to equal the *in-situ* CME transit time.

The initial CME density ($n_{0\mathrm{cme}}$), expressed by c in Equation (4), is a free parameter and it runs over a wide range of values (see Table 1). Large c values are associated with CMEs with large inertia, decreasing the SW effects on the CME dynamics. Thus, the larger the c value, the shorter the CME transit time (TT) and faster the arrival CME speed at 1 AU. Large values of c also have an impact on the shock propagation, causing shorter TTs and faster arrival shock speeds. The driving phase duration (Equation (2)) increases with c.

The value of $n_{0\mathrm{cme}}$ is difficult to approximate from the current observations, because it implies that one should know the coronal structure, the local density of the SW, the CME geometry and its total mass. The CME total mass has been estimated by employing Thomson scattering on coronagraph observations (Vourlidas *et al.*, 2000; Colaninno and Vourlidas, 2009) and also using extreme ultra-violet dimming (Aschwanden *et al.*, 2009). The total mass is related to Equations (6) and (18) and gives us a parameter to evaluate our initial conditions. In general, the c values that we used in Table 1 agree with the orders of magnitude of the CME total masses reported in studies commented on before.

The two-stages propagation for a fast CME/shock is consistent with empirical and numerical studies (*e.g.* Manoharan, 2006; Pohjolainen *et al.*, 2007 and González-Esparza *et al.*, 2003c). The analytic description for the shock evolution is dynamically and mathematically similar to the semi-empirical relation proposed by Pinter and Dryer (1990) for shocks associated with solar flares.

We discussed four fast halo CMEs (Earth-directed) simulating the type II radio drift emission associated with the IP shock. In all the cases, the calculated CME initial trajectories were consistent with LASCO data. The calculated arrival speeds and transit times of CMEs and shocks were quantitatively consistent with their *in-situ* measurements at 1 AU. According to our case study results (Table 2), the differences between the calculated and measured CME arrival speeds were less than 6 %; the differences for both shock arrival speeds and transit times were less than 5 %.

In our analytical model the CME injection time (Δt_f) represents the period when the CME acquires its initial kinetic energy and linear momentum (Cantó, Raga, and D'Alessio, 2000). We approximated this parameter as the flare rising phase, because that interval is associated with the time when the energetic CME reaches an almost constant speed (kinetic energy) in the coronagraph field of view (Zhang and Dere, 2006). Although it is widely accepted that CMEs are not necessarily related to solar flares (Gosling, 1993), some studies relate solar flares to the initiation of energetic CMEs. For example, Zhang *et al.* (2004) and Zhang and Dere (2006) found some relationships between soft X-ray fluxes and CME initial accelerations. On the other hand, Temmer *et al.* (2008) found a close synchronisation between the CME acceleration profiles and flare hard X-ray flux onsets. Furthermore, Chen and Kunkel (2010) found that the observed duration of soft X-ray emission is comparable to the poloidal flux injection, and such injection is related to the CME initial acceleration (Chen, 2001). Although in these studies a possible relation between the CME and flare initiation mechanisms appears, the authors also conclude that such relation is not trivial and requires further research. Since we are not aware of any observation that could directly provide us with the CME injection time, we choose the flare rising time as an equivalent; since, in our case, these energetic CMEs were associated with solar flares.

Our results suggest relations between the CME initial properties and the associated flare. Figure 6 shows the initial conditions for the seven fast CME events listed in Tables 1 and 2. Figure 6a presents the initial CME density with respect to the ambient wind (c) versus the flare rising time (Δt_f). The data points show the tendency that the flare rising time is inversely proportional to the CME density jump. In Figure 6b, the jump in CME-solar wind kinetic energy ($cv_{0\mathrm{cme}}^2/v_{1\mathrm{AU}}^2$) decreases as Δt_f increases:

$$c = 5.21\left[\frac{\Delta t_f}{1\ \mathrm{h}}\right]^{-0.82}, \tag{17}$$

$$c\frac{v_{0\mathrm{cme}}^2}{v_{1\mathrm{AU}}^2} = 44.18\left[\frac{\Delta t_f}{1\ \mathrm{h}}\right]^{-1.31}. \tag{18}$$

Although these tendencies were consistent for all the analysed events, we need to study a larger number of cases in order to corroborate the results. The trends in Equations (17) and (18) are in agreement with results of Zhang and Dere (2006). Zhang and Dere (2006), after having studied the initial acceleration of CMEs from coronagraph images, found that the stronger the "main" CME acceleration near the Sun ($a_{0\mathrm{cme}}$), the shorter the duration (Δt_a) of such acceleration. This relationship is expressed by $a_{0\mathrm{cme}}/1\ \mathrm{m\,s^{-2}} = 135.46(\Delta t_a/1\ \mathrm{h})^{-1.09}$, where $\Delta t_a \approx \Delta t_f$. Consequently, impulsive events (short Δt_f) tend to have more inertia and faster accelerations (*i.e.* larger relative kinetic energies). On the other hand, for gradual

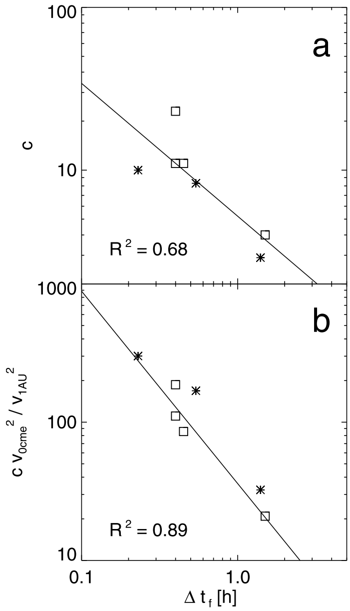

Figure 6 Relationships of the CME initial conditions and the solar flare rise time (Δt_f) of the events in Table 1. (a) Ratio between the CME and solar wind initial densities (Equation (4)) versus Δt_f. (b) Ratio between the CME and solar wind initial kinetic energies versus t_f. Open squares represent the four case studies. Solid lines are the best fit to the data.

events (long Δt_f) we expect the opposite tendency. This suggests that Δt_f might be related to the physical mechanisms by which a fast CME acquires its initial kinetic properties, in agreement with Zhang *et al.* (2004).

In this study we select the value of c to equal the calculated and reported transit times of CMEs. However, as we commented on before, c is difficult to measure directly from observations and we need an indirect method to estimate the initial kinetic properties of CMEs. In this sense, Equations (17) and (18) may be useful to approximate or to delimit the initial values for CME density and kinetic energy. Thus, it is important to develop further studies in order to corroborate or discard the mentioned relations.

In the seven events, the decaying stage began long before the shock reached 1 AU ($\sim 50 R_\odot \approx 0.25$ AU; see Table 2). Based on our model, this means that IP shocks associated with fast CMEs evolve like blast waves during most of their transit time to 1 AU. This result agrees with other studies. For example, Burlaga *et al.* (1981) pointed out, discussing linear momentum fluxes, that some CMEs may not drive shocks any more at distances around 2 AU. On the other hand, Feng *et al.* (2010) analysed the geometric properties of CME and shocks at 1 AU and concluded that at least 34 % of all shocks were not driven by their associated CMEs. Maloney and Gallagher (2011) measured standoff distances of fast CME/shocks within heliocentric ranges between $2 - 120 R_\odot$ and, in general, found them to be larger than expected. These results agree with an early onset of the decaying stage in CME/shock propagation.

We reproduce the radio frequency drift associated with the propagation of the IP shock. There are other studies comparing the evolution of CME/shock events and type II radio burst spectra detected by *Wind*/WAVES. Reiner, Kaiser, and Bougeret (2007) used an empirical model to calculate the arrival times of CME/shocks, assuming an initial strong deceleration followed by a constant speed propagation of the CME/shock (this constant speed is much faster than the ambient solar wind). Lara and Borgazzi (2009) assumed that the radio emission was associated with the propagation of the CME mass centre, the evolution of which was affected by viscosity and drag forces of the solar wind. What is different in our model is that we solve specifically both the CME and shock propagation. Then we calculate the type II frequency drift emission from the shock propagation solution. The CME and its shock suffer different heliocentric evolution, and propagate at different speeds. This becomes more significant when the magnetosonic Mach number is small, resulting in larger standoff distances and greater differences between the CME and the shock speeds and positions.

In all the case studies, the first harmonic of the simulated radio-burst emission agreed qualitatively with the lower part of the radio spectra detected by *Wind*/WAVES. This is somewhat similar to the study by Reiner, Kaiser, and Bougeret (2007), who used the first harmonic to adjust the CME/shock trajectories. However, in our case we match the lower part of the radio spectra. This former result is consistent with the study by Knock and Cairns (2005), who showed that the plasma frequency is a lower limit for the type II radio-burst emission, and the width of the spectra is related to the shock expansion and solar wind fluctuations. We do not take into account these two aspects in our model.

5. Conclusions

We analysed four fast CME halo events as case studies using an analytical model and compared the results with different data. The model implies two propagation stages for the CME and its shock. The dynamic processes between the CME and its shock wave are important to understand their heliocentric evolution. To perform the calculations we used different observations as initial conditions. In general, we found good agreement comparing the results and the CME/shock *in-situ* data at 1 AU. The first harmonic of the simulated radio-burst emission associated with the shock propagation was consistent with the lower part of the type II radio spectra detected by *Wind*/WAVES. The results of the analytical model imply that the shocks were not driven anymore by their CMEs when they reached 1 AU.

Acknowledgements P. Corona-Romero thanks CONACyT for the doctoral grant. J.A. Gonzalez-Esparza thanks for partial funding by projects DGAPA-PAPIIT (IN105310) and CONACyT (152471). E. Aguilar-Rodriguez thanks DGAPA-PAPIIT project (grant IN109112) and CONACyT project (grant 101625). The authors want to thank the referee, whose comments helped to significantly improve the presentation of this work.

Appendix

A.1 Polytropic MHD Jump Relations

Polytropic MHD jump relations are the specific jump relations used in this work; for a more general solution see Petrinec and Russell (1997), Equations (14), (15) and (16). The downstream variables (subindex 2) are related with their upstream counterparts (subindex 1) according to

$$\frac{1}{n_*} = \frac{\rho_1}{\rho_2} = -\frac{k_1}{k_9} - \frac{2^{1/3}k_3}{\mu_2^2 k_8 k_9} + \frac{k_8}{2^{1/3}\mu_2^2 k_9}, \tag{19}$$

$$B_* = \frac{|B_2|}{|B_1|} = \sqrt{c_{\theta 2}\left(1-\alpha^2\right)+\alpha^2}, \tag{20}$$

$$p_* = \frac{p_2}{p_1} = 1 + \left(1 - \frac{1}{n_*}\right)\frac{2\mu_2}{\beta} + \frac{1-c_{\theta 2}}{\beta}\left(1-\alpha^2\right). \tag{21}$$

In Equations (19), (20) and (21) we have used

$$
\begin{aligned}
c_{\theta 2} &= \cos^2(\theta_{Bn}),\\
\mu_2 &= M_{A1}^2,\\
\beta &= 2\mu_0 \frac{p_1}{B_1^2},\\
\alpha &= \frac{c_{\theta 2} - \mu_2}{c_{\theta 2} - \mu_2/n_*},\\
k_1 &= -\gamma(1+\beta) + \mu_2(1-\gamma) - c_{\theta 2}(2+\gamma),\\
k_2 &= \mu_2(-2+\gamma) + c_{\theta 2}\bigl(1+\gamma[1+2\beta+\mu_2]\bigr),\\
k_3 &= \mu_2^4\bigl(-k_1^2 + 3[1+\gamma]k_2\bigr),\\
k_4 &= \mu_2(1-\gamma) - \beta\gamma c_{\theta 2},\\
k_5 &= 9(1+\gamma)\mu_2^6 k_1 k_2,\\
k_6 &= -2\mu_2^6 k_1^3 - 27(1+\gamma)^2\mu_2^6 c_{\theta 2} k_4 + k_5,\\
k_7 &= \bigl(4k_3^3 + k_6^2\bigr)^{1/2},\\
k_8 &= (k_6 + k_7)^{1/3},\\
k_9 &= 3(1+\gamma)\mu_2.
\end{aligned}
$$

To obtain Equations (19), (20) and (21) we assume that the normal to the shock is radial at the shock front.

A.2 Velocity Coplanarity

The velocity coplanarity is commonly used to approximate the shock velocity by applying the mass conservation at the shock reference frame. If a shock wave propagates with a velocity $\mathbf{v}_{\text{sh}}$ through an ambient solar wind with density ρ_1 and velocity $\mathbf{v}_1$, the shock wave velocity shall fulfil $\rho_1(\mathbf{v}_{\text{sh}} - \mathbf{v}_1) = \rho_2(\mathbf{v}_{\text{sh}} - \mathbf{v}_2)$, where the subindex 2 indicates the downstream values. Thus, solving for $\mathbf{v}_{\text{sh}}$:

$$\mathbf{v}_{\text{sh}} = \frac{\rho_2\mathbf{v}_2 - \rho_1\mathbf{v}_1}{\rho_2 - \rho_1}. \tag{22}$$

References

Aschwanden, M.J., Nitta, N.V., Wuelser, J.-P., Lemen, J.R., Sandman, A., Vourlidas, A., Colaninno, R.C.: 2009, First measurements of the mass of coronal mass ejections from the EUV dimming observed with STEREO EUVI A+B spacecraft. *Astrophys. J.* **706**, 376 – 392. doi:10.1088/0004-637X/706/1/376.

Bisi, M.M., Breen, A.R., Jackson, B.V., Fallows, R.A., Walsh, A.P., Mikić, Z., Riley, P., Owen, C.J., Gonzalez-Esparza, A., Aguilar-Rodriguez, E., Morgan, H., Jensen, E.A., Wood, A.G., Owens, M.J., Tokumaru, M., Manoharan, P.K., Chashei, I.V., Giunta, A.S., Linker, J.A., Shishov, V.I., Tyul'Bashev, S.A., Agalya, G., Glubokova, S.K., Hamilton, M.S., Fujiki, K., Hick, P.P., Clover, J.M., Pintér, B.: 2010, From the Sun to the Earth: The 13 May 2005 coronal mass ejection. *Solar Phys.* **265**, 49 – 127. doi:10.1007/s11207-010-9602-8.

Borgazzi, A., Lara, A., Echer, E., Alves, M.V.: 2009, Dynamics of coronal mass ejections in the interplanetary medium. *Astron. Astrophys.* **498**, 885 – 889. doi:10.1051/0004-6361/200811171.

Bothmer, V., Schwenn, R.: 1998, The structure and origin of magnetic clouds in the solar wind. *Ann. Geophys.* **16**, 1 – 24. doi:10.1007/s005850050575.

Bougeret, J.-L., Kaiser, M.L., Kellogg, P.J., Manning, R., Goetz, K., Monson, S.J., Monge, N., Friel, L., Meetre, C.A., Perche, C., Sitruk, L., Hoang, S.: 1995, Waves: The radio and plasma wave investigation on the Wind spacecraft. *Space Sci. Rev.* **71**, 231 – 263. doi:10.1007/BF00751331.

Burlaga, L., Sittler, E., Mariani, F., Schwenn, R.: 1981, Magnetic loop behind an interplanetary shock – Voyager, Helios, and IMP 8 observations. *J. Geophys. Res.* **86**, 6673 – 6684. doi:10.1029/JA086iA08p06673.

Cane, H.V., Stone, R.G.: 1984, Type II solar radio bursts, interplanetary shocks, and energetic particle events. *Astrophys. J.* **282**, 339 – 344. doi:10.1086/162207.

Cane, H.V., Sheeley, N.R. Jr., Howard, R.A.: 1987, Energetic interplanetary shocks, radio emission, and coronal mass ejections. *J. Geophys. Res.* **92**, 9869 – 9874. doi:10.1029/JA092iA09p09869.

Cantó, J., Raga, A.C., D'Alessio, P.: 2000, Analytic solutions to the problem of jets with time-dependent injection velocities. *Mon. Not. Roy. Astron. Soc.* **313**, 656 – 662. doi:10.1046/j.1365-8711.2000.03244.x.

Cantó, J., González, R.F., Raga, A.C., de Gouveia Dal Pino, E.M., Lara, A., González-Esparza, J.A.: 2005, The dynamics of velocity fluctuations in the solar wind – I. Coronal mass ejections. *Mon. Not. Roy. Astron. Soc.* **357**, 572 – 578. doi:10.1111/j.1365-2966.2005.08670.x.

Cargill, P.J.: 2004, On the aerodynamic drag force acting on interplanetary coronal mass ejections. *Solar Phys.* **221**, 135 – 149. doi:10.1023/B:SOLA.0000033366.10725.a2.

Cavaliere, A., Messina, A.: 1976, Propagation of blast waves. *Astrophys. J.* **209**, 424 – 428. doi:10.1086/154736.

Chen, J.: 2001, Physics of coronal mass ejections: A new paradigm of solar eruptions. *Space Sci. Rev.* **95**, 165 – 190.

Chen, J., Kunkel, V.: 2010, Temporal and physical connection between coronal mass ejections and flares. *Astrophys. J.* **717**, 1105 – 1122. doi:10.1088/0004-637X/717/2/1105.

Cho, K.-S., Moon, Y.-J., Dryer, M., Fry, C.D., Park, Y.-D., Kim, K.-S.: 2003, A statistical comparison of interplanetary shock and CME propagation models. *J. Geophys. Res.* **108**, 1445. doi:10.1029/2003JA010029.

Colaninno, R.C., Vourlidas, A.: 2009, First determination of the true mass of coronal mass ejections: A novel approach to using the two STEREO viewpoints. *Astrophys. J.* **698**, 852 – 858. doi:10.1088/0004-637X/698/1/852.

Corona-Romero, P., Gonzalez-Esparza, J.A.: 2011, Numeric and analytic study of interplanetary coronal mass ejection and shock evolution: Driving, decoupling, and decaying. *J. Geophys. Res.* **116**, 5104. doi:10.1029/2010JA016008.

Dryer, M.: 1974, Interplanetary shock waves generated by solar flares. *Space Sci. Rev.* **15**, 403 – 468. doi:10.1007/BF00178215.

Farris, M.H., Russell, C.T.: 1994, Determining the standoff distance of the bow shock: Mach number dependence and use of models. *J. Geophys. Res.* **99**, 17681. doi:10.1029/94JA01020.

Feng, H.Q., Wu, D.J., Chao, J.K., Lee, L.C., Lyu, L.H.: 2010, Are all leading shocks driven by magnetic clouds? *J. Geophys. Res.* **115**, 4107. doi:10.1029/2009JA014875.

Forbes, T.G., Linker, J.A., Chen, J., Cid, C., Kóta, J., Lee, M.A., Mann, G., Mikić, Z., Potgieter, M.S., Schmidt, J.M., Siscoe, G.L., Vainio, R., Antiochos, S.K., Riley, P.: 2006, CME theory and models. *Space Sci. Rev.* **123**, 251 – 302. doi:10.1007/s11214-006-9019-8.

Forsyth, R.J., Bothmer, V., Cid, C., Crooker, N.U., Horbury, T.S., Kecskemety, K., Klecker, B., Linker, J.A., Odstrcil, D., Reiner, M.J., Richardson, I.G., Rodriguez-Pacheco, J., Schmidt, J.M., Wimmer-Schweingruber, R.F.: 2006, ICMEs in the Inner Heliosphere: Origin, evolution and propagation effects. Report of Working Group G. *Space Sci. Rev.* **123**, 383 – 416. doi:10.1007/s11214-006-9022-0.

González, R.F., Cantó, J.: 2002, Radio-continuum emission from shocked stellar winds in low-mass stars. *Astrophys. J.* **580**, 459 – 467. doi:10.1086/343037.

González, R.F., Montes, G., Cantó, J., Loinard, L.: 2006, Predicted radio-continuum emission from the little Homunculus of the η Carinae nebula. *Mon. Not. Roy. Astron. Soc.* **373**, 391 – 396. doi:10.1111/j.1365-2966.2006.11055.x.

Gonzalez-Esparza, A., Aguilar-Rodriguez, E.: 2009, Speed evolution of fast CME/shocks with SOHO/LASCO, WIND/WAVES, IPS and in-situ WIND data: analysis of kilometric type-II emissions. *Ann. Geophys.* **27**, 3957 – 3966. doi:10.5194/angeo-27-3957-2009.

González-Esparza, J.A., Jeyakumar, S.: 2007, Propagation and interaction of interplanetary transient disturbances. Numerical simulations. *Adv. Space Res.* **40**, 1815 – 1820. doi:10.1016/j.asr.2007.06.021.

González-Esparza, J.A., Lara, A., Pérez-Tijerina, E., Santillán, A., Gopalswamy, N.: 2003a, A numerical study on the acceleration and transit time of coronal mass ejections in the interplanetary medium. *J. Geophys. Res.* **108**, 1039. doi:10.1029/2001JA009186.

González-Esparza, J.A., Lara, A., Santillán, A., Gopalswamy, N.: 2003b, A numerical study on the evolution of CMEs and shocks in the interplanetary medium. In: Velli, M., Bruno, R., Malara, F., Bucci, B. (eds.) *Solar Wind Ten*, *Am. Inst. Phys. Conf. Ser.* **679**, 206 – 209. doi:10.1063/1.1618578.

González-Esparza, J.A., Cantó, J., González, R.F., Lara, A., Raga, A.C.: 2003c, Propagation of CMEs in the interplanetary medium: Numerical and analytical results. *Adv. Space Res.* **32**, 513 – 518. doi:10.1016/S0273-1177(03)00334-X.

Gopalswamy, N., Kaiser, M.L., Lepping, R.P., Kahler, S.W., Ogilvie, K., Berdichevsky, D., Kondo, T., Isobe, T., Akioka, M.: 1998, Origin of coronal and interplanetary shocks – A new look with WIND spacecraft data. *J. Geophys. Res.* **103**, 307. doi:10.1029/97JA02634.

Gopalswamy, N., Lara, A., Lepping, R.P., Kaiser, M.L., Berdichevsky, D., St. Cyr, O.C.: 2000, Interplanetary acceleration of coronal mass ejections. *Geophys. Res. Lett.* **27**, 145 – 148. doi:10.1029/1999GL003639.

Gopalswamy, N., Lara, A., Manoharan, P.K., Howard, R.A.: 2005, An empirical model to predict the 1-AU arrival of interplanetary shocks. *Adv. Space Res.* **36**, 2289 – 2294. doi:10.1016/j.asr.2004.07.014.

Gopalswamy, N., Yashiro, S., Akiyama, S., Mäkelä, P., Xie, H., Kaiser, M.L., Howard, R.A., Bougeret, J.L.: 2008, Coronal mass ejections, type II radio bursts, and solar energetic particle events in the SOHO era. *Ann. Geophys.* **26**, 3033 – 3047. doi:10.5194/angeo-26-3033-2008.

Gopalswamy, N., Yashiro, S., Michalek, G., Stenborg, G., Vourlidas, A., Freeland, S., Howard, R.: 2009, The SOHO/LASCO CME catalog. *Earth Moon Planets* **104**, 295 – 313. doi:10.1007/s11038-008-9282-7.

Gosling, J.T.: 1993, The solar flare myth. *J. Geophys. Res.* **98**, 18937 – 18950. doi:10.1029/93JA01896.

Harrison, R.A., Davis, C.J., Eyles, C.J., Bewsher, D., Crothers, S.R., Davies, J.A., Howard, R.A., Moses, D.J., Socker, D.G., Newmark, J.S., Halain, J.-P., Defise, J.-M., Mazy, E., Rochus, P., Webb, D.F., Simnett, G.M.: 2008, First imaging of coronal mass ejections in the heliosphere viewed from outside the Sun Earth line. *Solar Phys.* **247**, 171 – 193. doi:10.1007/s11207-007-9083-6.

Kim, K.-H., Moon, Y.-J., Cho, K.-S.: 2007, Prediction of the 1-AU arrival times of CME-associated interplanetary shocks: Evaluation of an empirical interplanetary shock propagation model. *J. Geophys. Res.* **112**, 5104. doi:10.1029/2006JA011904.

Knock, S.A., Cairns, I.H.: 2005, Type II radio emission predictions: Sources of coronal and interplanetary spectral structure. *J. Geophys. Res.* **110**.

Lara, A., Borgazzi, A.I.: 2009, Dynamics of interplanetary CMEs and associated type II bursts. In: Gopalswamy, N., Webb, D.F. (eds.) *IAU Symp.* **257**, 287 – 290. doi:10.1017/S1743921309029421.

Liu, Y., Davies, J.A., Luhmann, J.G., Vourlidas, A., Bale, S.D., Lin, R.P.: 2010a, Geometric triangulation of imaging observations to track coronal mass ejections continuously out to 1 AU. *Astrophys. J. Lett.* **710**, L82 – L87. doi:10.1088/2041-8205/710/1/L82.

Liu, Y., Thernisien, A., Luhmann, J.G., Vourlidas, A., Davies, J.A., Lin, R.P., Bale, S.D.: 2010b, Reconstructing coronal mass ejections with coordinated imaging and in situ observations: Global structure, kinematics, and implications for space weather forecasting. *Astrophys. J.* **722**, 1762 – 1777. doi:10.1088/0004-637X/722/2/1762.

Maloney, S.A., Gallagher, P.T.: 2011, STEREO direct imaging of a coronal mass ejection-driven shock to 0.5 AU. *Astrophys. J. Lett.* **736**, L5. doi:10.1088/2041-8205/736/1/L5.

Manoharan, P.K.: 2006, Evolution of coronal mass ejections in the Inner Heliosphere: A study using white-light and scintillation images. *Solar Phys.* **235**, 345 – 368. doi:10.1007/s11207-006-0100-y.

Manoharan, P.K.: 2010, Ooty interplanetary scintillation – Remote-sensing observations and analysis of coronal mass ejections in the heliosphere. *Solar Phys.* **265**, 137 – 157. doi:10.1007/s11207-010-9593-5.

Manoharan, P.K., Tokumaru, M., Pick, M., Subramanian, P., Ipavich, F.M., Schenk, K., Kaiser, M.L., Lepping, R.P., Vourlidas, A.: 2001, Coronal mass ejection of 2000 July 14 flare event: Imaging from near-Sun to Earth environment. *Astrophys. J.* **559**, 1180 – 1189. doi:10.1086/322332.

Nakajima, H., Kawashima, S., Shinohara, N., Shiomi, Y., Enome, S., Rieger, E.: 1990, A high-speed shock wave in the impulsive phase of 1984 April 24 flare. *Astrophys. J. Suppl. Ser.* **73**, 177 – 183. doi:10.1086/191449.

Ontiveros, V., Gonzalez-Esparza, J.A.: 2010, Geomagnetic storms caused by shocks and ICMEs. *J. Geophys. Res.* **115**, 10244. doi:10.1029/2010JA015471.

Ontiveros, V., Vourlidas, A.: 2009, Quantitative measurements of coronal mass ejection-driven shocks from LASCO observations. *Astrophys. J.* **693**, 267 – 275. doi:10.1088/0004-637X/693/1/267.

Petrinec, S.M.: 2002, The location of the Earth's bow shock. *Planet. Space Sci.* **50**, 541 – 547. doi:10.1016/S0032-0633(02)00033-8.

Petrinec, S.M., Russell, C.T.: 1997, Hydrodynamic and MHD equations across the bow shock and along the surfaces of planetary obstacles. *Space Sci. Rev.* **79**, 757 – 791. doi:10.1023/A:1004938724300.

Pinter, S., Dryer, M.: 1990, Conversion of piston-driven shocks from powerful solar flares to blast waves in the solar wind. *Bull. Astron. Inst. Czechoslov.* **41**, 137 – 148.

Pohjolainen, S., van Driel-Gesztelyi, L., Culhane, J.L., Manoharan, P.K., Elliott, H.A.: 2007, CME propagation characteristics from radio observations. *Solar Phys.* **244**, 167 – 188. doi:10.1007/s11207-007-9006-6.

Reiner, M.J., Kaiser, M.L., Bougeret, J.-L.: 2007, Coronal and interplanetary propagation of CME/shocks from radio, in situ and white-light observations. *Astrophys. J.* **663**, 1369 – 1385. doi:10.1086/518683.

Richardson, I.G., Cane, H.V.: 2010, Near-Earth interplanetary coronal mass ejections during solar cycle 23 (1996 – 2009): Catalog and summary of properties. *Solar Phys.* **264**, 189 – 237. doi:10.1007/s11207-010-9568-6.

Smart, D.F., Shea, M.A.: 1985, A simplified model for timing the arrival of solar flare-initiated shocks. *J. Geophys. Res.* **90**, 183 – 190. doi:10.1029/JA090iA01p00183.

Tappin, S.J.: 2006, The deceleration of an interplanetary transient from the Sun to 5 AU. *Solar Phys.* **233**, 233 – 248. doi:10.1007/s11207-006-2065-2.

Temmer, M., Veronig, A.M., Vršnak, B., Rybák, J., Gömöry, P., Stoiser, S., Maričić, D.: 2008, Acceleration in fast halo CMEs and synchronized flare HXR bursts. *Astrophys. J. Lett.* **673**, L95 – L98. doi:10.1086/527414.

Vourlidas, A., Ontiveros, V.: 2009, A review of coronagraphic observations of shocks driven by coronal mass ejections. In: Ao, X., Burrows, G.Z.R. (eds.) *American Institute of Physics Conference Series* **1183**, 139 – 146. doi:10.1063/1.3266770.

Vourlidas, A., Subramanian, P., Dere, K.P., Howard, R.A.: 2000, Large-angle spectrometric coronagraph measurements of the energetics of coronal mass ejections. *Astrophys. J.* **534**, 456 – 467. doi:10.1086/308747.

Vršnak, B.: 2006, Forces governing coronal mass ejections. *Adv. Space Res.* **38**, 431 – 440. doi:10.1016/j.asr.2005.03.090.

Vršnak, B.: 2008, Processes and mechanisms governing the initiation and propagation of CMEs. *Ann. Geophys.* **26**, 3089 – 3101. doi:10.5194/angeo-26-3089-2008.

Vršnak, B., Gopalswamy, N.: 2002, Influence of the aerodynamic drag on the motion of interplanetary ejecta. *J. Geophys. Res.* **107**, 1019. doi:10.1029/2001JA000120.

Vršnak, B., Ruzdjak, V., Zlobec, P., Aurass, H.: 1995, Ignition of MHD shocks associated with solar flares. *Solar Phys.* **158**, 331 – 351. doi:10.1007/BF00795667.

Webb, D.F., Gopalswamy, N.: 2006, Coronal mass ejections and space weather. In: Gopalswamy, N., Bhattacharyya, A. (eds.) *Proceedings of the ILWS Workshop*, 71.

Webb, D.F., Biesecker, D., Howard, T.A., Luhmann, J.G., Li, Y., Galvin, A., Howard, R.A., Jackson, B.V.: 2009a, CMEs in the heliosphere observed with combined imaging and *in-situ* data from LASCO, Stereo and SMEI. In: *AAS/Solar Physics Division Meeting* **40**, #21.02.

Webb, D.F., Howard, T.A., Fry, C.D., Kuchar, T.A., Odstrcil, D., Jackson, B.V., Bisi, M.M., Harrison, R.A., Morrill, J.S., Howard, R.A., Johnston, J.C.: 2009b, Study of CME propagation in the Inner Heliosphere: SOHO LASCO, SMEI and STEREO HI observations of the January 2007 events. *Solar Phys.* **256**, 239 – 267. doi:10.1007/s11207-009-9351-8.

Zhang, J., Dere, K.P.: 2006, A statistical study of main and residual accelerations of coronal mass ejections. *Astrophys. J.* **649**, 1100 – 1109. doi:10.1086/506903.

Zhang, J., Dere, K.P., Howard, R.A., Vourlidas, A.: 2004, A study of the kinematic evolution of coronal mass ejections. *Astrophys. J.* **604**, 420 – 432. doi:10.1086/381725.